Optics Letters

Liquid crystal integrated metalens with dynamic focusing property

Shenghang Zhou,[1,†] Zhixiong Shen,[1,2,†] Xinan Li,[1] Shijun Ge,[1,2,3] Yanqing Lu,[1] and Wei Hu[1,2,*]

[1]National Laboratory of Solid State Microstructures, Key Laboratory of Intelligent Optical Sensing and Manipulation, College of Engineering and Applied Sciences, and Collaborative Innovation Center of Advanced Microstructures, Nanjing University, Nanjing 210093, China
[2]Institute for Smart Liquid Crystals, JITRI, Changshu 215500, China
[3]e-mail: geshijun@nju.edu.cn
*Corresponding author: huwei@nju.edu.cn

Received 27 May 2020; revised 17 June 2020; accepted 30 June 2020; posted 30 June 2020 (Doc. ID 398601); published 30 July 2020

Metalenses are developing fast towards versatile and integrated terahertz (THz) apparatuses, while tunable ones are highly pursued. Here, we propose a strategy that integrates dielectric metasurfaces with liquid crystals (LCs) to realize the dynamic focal spot manipulation. The silicon pillar meta-units of the metasurface are properly selected to generate different phase profiles for two orthogonal linear polarizations, permitting a laterally or axially altered focal spot. After LCs integrated, polarization-multiplexed focusing can be achieved via electrically varying the LC orientations. We demonstrate two metalenses with distinct functions. For the first one, the uniformly aligned LC works as a polarization converter, and further switches the focal length by altering the bias. For the second one, an LC polarization grating is utilized for rear spin-selective beam deflection. Consequently, a THz port selector is presented. This work supplies a promising method towards active THz elements, which may be widely applied in THz sensing, imaging, and communication.

https://doi.org/10.1364/OL.398601

At present, the fifth-generation (5G) wireless network is under construction all over the world. To further accelerate the communications, fundamental research towards future techniques is investigated meanwhile [1,2]. The carrier frequency of the terahertz (THz) band is several orders higher than the radio frequency (RF) band, thus it is promising to meet the requirement of the fast-increasing channel capacity [3]. However, "THz gap" is the last explored one in the electromagnetic spectrum, and corresponding THz devices are far from maturation. The lens plays a vital role in communications for beam coupling, focusing, and collimating. The conventional reflective parabola mirrors and refractive lenses work on the cumulative phase, suffering from their bulky architectures [4]. A metalens is able to introduce an abrupt phase change via elaborately designing the subwavelength metallic or dielectric meta-units, which supplies a planar way for versatile wavefront manipulations [5–7], including spin-selected, broadband achromatic, and super-resolution focusing [8–11]. The dielectric metalens is more attractive compared with the metallic counterparts thanks to the enhanced efficiency and CMOS-compatible manufacturing [12,13]. Once the lens is fabricated, the function remains static, limiting its practical applications. Recently, enormous efforts have been paid to achieve the active tuning of THz metasurfaces. Semiconductors, graphene, phase-change materials, and superconductors have been reported to integrate with them [14–17]. Nevertheless, most of these metadevices have uniform meta-unit arrays. As a result, their tunability is limited to spectra, while the more promising tunable functions are still urgent tasks.

Thanks to the large broadband birefringence from the visible to microwave and excellent electro-optical responsivity, liquid crystals (LCs) are widely applied in various optical fields including displays, specific optical beam generations, tunable color filters and spatial light modulators [18–20]. Until recently, two main obstacles that restrict the application of LCs in the THz regime have been settled, i.e., high-transparency THz electrodes and photopatterning techniques for thick cells (up to hundreds of microns) [21]. A homogeneously aligned LC cell can act as a tunable THz phase shifter or waveplate. Through encoding geometric phases into the LC orientations, more fascinating functions, e.g., vortex beam generators and spin-selected lenses, have been developed [22,23]. These devices can modulate the phase front with external field stimulated tunability and circular polarization selectivity. If one can integrate the above-mentioned THz LC components with metasurfaces, the freedom of function tunability will be thoroughly released. Unfortunately, relevant researches are rarely documented in the THz band.

Here, we integrate LCs with metalenses and demonstrate dynamic THz lenses with position controllable focal spots. The device is composed of a silicon pillar array and an LC layer separated by graphene electrodes. The metasurface works as both a dual-focal lens and one substrate of LC layer. The LC layer is pre-aligned, and its orientations can be further electrically tuned. Two LC integrated metalenses are presented: the first one is an LC waveplate integrated metalens with polarization-dependent focal length, while the second one is a combination

of a lens with laterally mirrored focal spots and a rear LC polarization grating. These metalenses provide controllable focal spots that can be dynamically tuned with bias. It may supply a promising strategy for multifunctional and active tuning THz metalenses.

The geometry of the silicon pillar meta-unit is schematically illustrated in Fig. 1(a). When the THz wave propagates along z-axis, each pillar can be regarded as an effective waveguide. The phase of the transmitted wave is given by $n_{\text{eff}} \cdot h \cdot 2\pi/\lambda$, where n_{eff}, h, and λ are the effective refractive index of the waveguide mode, the pillar height, and the incident wavelength, respectively. Obviously, the phase increases linearly with the frequency. If the structure of the pillar is asymmetric along l and w, the n_{eff} is different for E_x and E_y incidences, which enables the polarization-dependent phase shifts. Simulations on the meta-unit waveguide are carried out with a commercial software Lumerical FDTD Solutions. The refractive index of high-resistance silicon is set as $n_{\text{Si}} = 3.45$ at 1.0 THz. Periodic boundary conditions are set on both x- and y-axes and a perfectly matched layer is set on z-axis. As an example, Fig. 1(b) depicts the dependency of the simulated resonant phase on the frequency under E_x and E_y incidences, separately. Their dependencies of phase on frequency are approximately linear. Due to the different value between w and l, the resonant phase varies a little for orthogonal polarizations. The side views of the normalized magnetic power at 1.0 THz under E_x and E_y incidences are presented, where two distinct resonance modes confined in the pillar are observed.

We fix $h = 200$ μm, $p = 150$ μm, and the target frequency of 1.0 THz, and then vary l and w (both from 20 to 120 μm) to achieve structural databases on the phase [Fig. 1(c)] and the transmittance [Fig. 1(d)], respectively, for E_x incidence. The case for E_y is diagonally symmetric to that of E_x. We can properly select the pillar geometries to simultaneously achieve the desired phase distributions for E_x and E_y incidences. Through rational design of the metasurface, arbitrary polarization-dependent wavefront manipulation could be realized. The criterion for a transmittance over 0.7 of each pillar is set to optimize the efficiency. In this way, devices with polarization-dependent phase modulations can be efficiently realized.

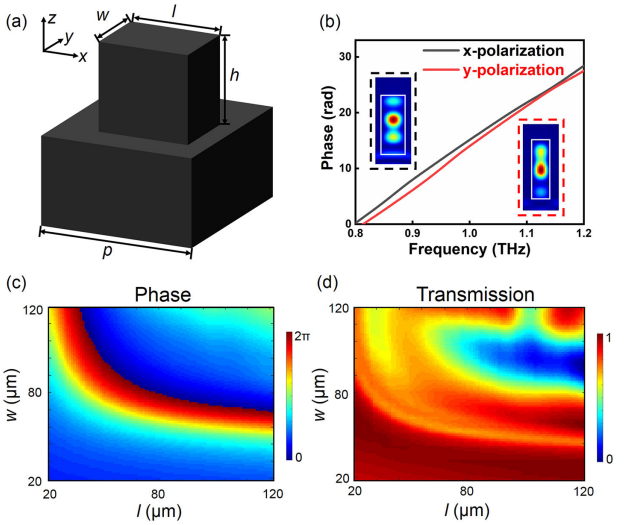

Fig. 1. Principle of the polarization-dependent dielectric metasurface. (a) Schematic of the silicon pillar meta-unit. (b) Frequency dependent resonant phase of the pillar with $l = 80$ μm and $w = 60$ μm under x- (black) and y- (red) incident polarizations. The insets show the normalized magnetic power in the xz-plane under the E_x incidence (black dashed box) and yz-plane under E_y incidence (red dashed box). (c), (d) Dependencies of (c) the phase and (d) the transmission of silicon pillars on l and w under E_x incidence at 1.0 THz.

To demonstrate the polarization-dependent focusing, a dual-focal lens with different focal lengths with respect to E_x and E_y incidences is designed and fabricated. The phase profile is written as

$$\varphi_{\text{Lens1}} = -\frac{2\pi}{\lambda}\left(\sqrt{f_{i,j}{}^2 + x^2 + y^2} - f_{i,j}\right), \tag{1}$$

where the subscripts i and j indicate the E_x and E_y incidences. Here, f_i and f_j are designed as 12.0 mm and 16.0 mm, respectively. Figure 2(a) shows the photograph of the metasurface, which reveals a radially symmetric geometry. The scanning electron microscope (SEM) image in Fig. 2(b) exhibits a zoom-in image of the region marked in Fig. 2(a), in which the varying geometries of different well-defined micro pillars are clearly observed. To verify the design, a numerical simulation of the lens is carried out. Due to the geometric symmetry of the lens, only a case along one radius is simulated. Figure 2(c) shows the simulated intensity distributions under E_x and E_y incidences. The simulated f_i and f_j are 12.2 mm and 15.9 mm, respectively, which are consistent with the design.

To endow the metalens with a tunability, a homogeneous LC waveplate is integrated and electrically switched, as schematically shown in Figs. 2(d) and 2(e). It is a uniformly aligned LC layer sandwiched by a fused silica and the metasurface, both of which are covered by a few-layer graphene transparent electrode and followed by a thin photoalignment layer. The LC orientation is set as 45° with respect to the E_x. The THz phase retardation induced by the waveplate is expressed by

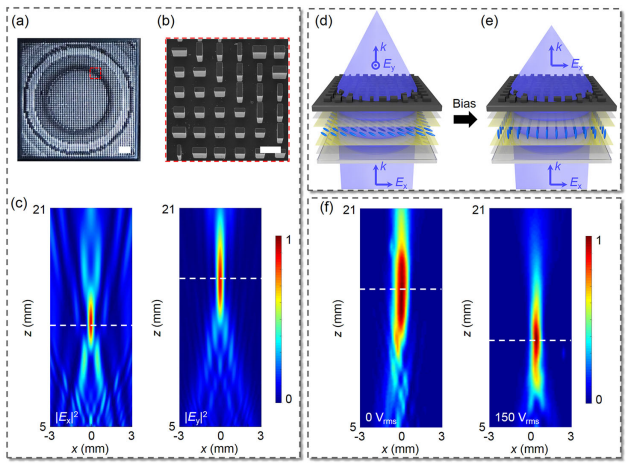

Fig. 2. LC waveplate integrated metalens for dynamic focal length manipulation. (a) Photograph of the metalens. (b) A zoom-in SEM image of silicon pillars labeled by the red square in (a). Scale bars in (a) and (b) are 1 mm and 150 μm, respectively. (c) Simulated THz intensity distributions in the xz-plane at 1.0 THz for E_x (left) and E_y (right) incidences, separately. (d), (e) Schematic focal length variation of the LC integrated metalens at (d) bias OFF and (e) bias saturated state, respectively. (f) Measured intensity distributions in the xz-plane at 1.0 THz at 0 V_{rms} (left) and 150 V_{rms} (right), separately.

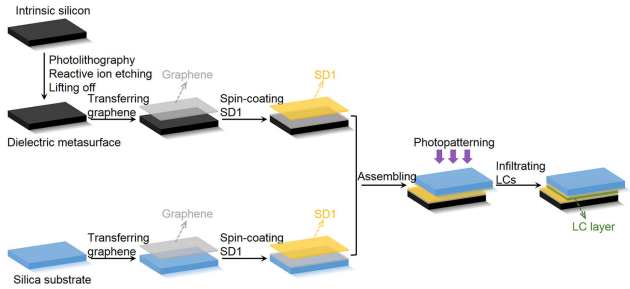

Fig. 3. Fabrication process of the LC integrated metalens.

$\Delta\varphi = \Delta n \cdot d \cdot 2\pi/\lambda$, where Δn denotes the birefringence, and d is the cell gap. When the applied voltage increases from none to saturated, LCs gradually stand up and finally orient along z-axis. It contributes to a continuous decrease of Δn and subsequent $\Delta\varphi$, causing the evolution of output polarizations. Here, d is set as 500 μm to achieve the half-wave condition at 1.0 THz.

As schematically shown in Fig. 3, the fabrication of the LC integrated metalens is briefly introduced. The metasurface is fabricated via a standard photolithography process followed by a reactive ion etching on a 500-μm-thick high-resistance silicon wafer. Then the residual photoresist is lifted off. Both the metasurface and the fused silica substrates are ultrasonically cleaned and O-plasma treated. Then the few-layer graphene films are transferred to them from copper foil (Six Carbon Technology, Shenzhen, China). After that, both substrates are spin-coated with an SD1 [24,25] photoalignment agent (Dai-Nippon Ink and Chemicals, Chiba, Japan). Then the metasurface and silica substrate are assembled and separated by a 500-μm-thick Mylar spacer to form a cell. It is exposed under a linearly polarized UV light to carry out the uniform alignment. Then the LC NJU-LDn-4 with a birefringence of 0.3 at 1.0 THz is infiltrated to form the desired LC orientation.

A scanning near-field THz microscope (SNTM) setup [26], which is based on the photoconductive THz emission and detection, is utilized to characterize the performance of the LC integrated metalens. The setup can scan both the intensity and the phase of the THz wavefront point by point in three dimensions with an interval of 0.2 mm. The measured intensity distributions in the xz-plane at 0 V_{rms} and 150 V_{rms} are shown in Fig. 2(f). At bias OFF state, the incident E_x is converted to E_y and focused at $z = 15.1$ mm. When the saturated bias of 150 V_{rms} (1 kHz square-wave) is applied, the E_x remains unchanged after passing the LC layer, contributing to the other $f = 11.3$ mm. Slight deviations of the focal length and the focal spot size are observed. They are attributed to two reasons. The first one is the fabrication error, especially the etching depth error, resulting in an imperfect lens phase profile. The second one is the scattering induced by the thick LC cell and the nonuniform graphene electrodes, which may enlarge the focal spot. By optimizing the etching cycles and adopting other materials with better uniformity, the focusing property can be improved.

To demonstrate the versatility of the LC integrated metalens, we design another metalens with mirrored focal spots with respect to y-axis under E_x and E_y incidences. The phase profile is expressed as

$$\varphi_{\text{Lens2}} = -\frac{2\pi}{\lambda}\left(\sqrt{f^2 + (x \pm t)^2 + y^2} - f\right), \quad (2)$$

where t is a displacement on x-axis. Its sign is dependent on the incident polarization, where + is for E_x, and—is for E_y incidence, respectively. This lens can focus E_x and E_y to designed $f = 12.0$ mm with opposite $t = \pm 2.0$ mm. The photograph in Fig. 4(a) vividly shows the symmetric morphology of the fabricated sample. Simulated intensity distributions for E_x and E_y incidences are shown in Fig. 4(b). Both focal lengths are 12.0 mm, which is consistent with the design.

Further introducing LC waveplates with spatially variant director distributions, more fascinating functions can be achieved. Here, a geometric phase (GP) based LC polarization grating (PG) is integrated to the above metalens to achieve a dynamic focal spot selection. GP originates from the photonic spin-orbit interaction. For the circular polarization (CP) incidence, a full phase control ($0-2\pi$) of a CP-converted THz wave can be realized when the orientation angle continuously changes from 0 to π. The photopatterning technique enables an arbitrary GP generation. As schematically shown in Fig. 4(c), the LC director is periodically varied along the y-axis to form a blazed GP modulation, which can deflect the orthogonal CP components to two opposite deflection angles. The designed phase of the PG is written as

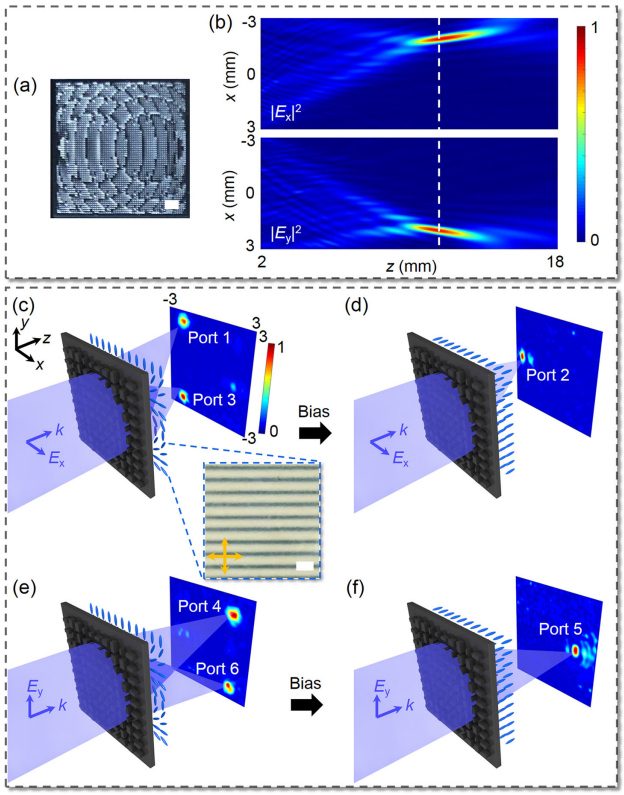

Fig. 4. LC PG integrated metalens for active port selection. (a) Photograph of the metasurface. Scale bar: 1 mm. (b) Simulated intensity distributions in the xz-plane at 1.0 THz under E_x (up) and E_y (down) incidences. (c)–(f) Schematic dynamic focal spot manipulations and measured intensity distributions at the focal plane ($z = 12.0$ mm) at 1.0 THz under E_x incidence at (c) bias OFF and (d) bias saturated states, and under E_y incidence at (e) bias OFF and (f) bias saturated states, respectively. The inset in (c) shows the photograph of the LC PG under crossed polarizers (indicated by two orange arrows). Scale bar: 1 mm.

$$\varphi_{PG} = -\frac{2\pi}{\lambda} y \sin\theta, \quad (3)$$

where y is the position along the grating vector of PG, and θ is the deflection angle (designed as 12.0° at 1.0 THz). d of PG is 500 μm to eliminate the zeroth order diffraction. The inset of Fig. 4(c) presents the photograph of the LC PG, where periodic black and white stripes consistent with the LC director variation are observed. To realize the desired LC orientation, a digital micro-mirror device-based dynamic microlithography setup is utilized to perform a multi-step partly-overlapping exposure [23].

Such a metadevice can serve as a THz port selector, which focuses the incident wave to certain different channels. As shown in Fig. 4(c), at bias OFF state, the incident E_x wave is focused to the left side and splits to two spots mirrored along the x-axis as the E_x contains equal left/right CP components (E_L/E_R). Thus port 1 (E_L) and 3 (E_R) are selected. When saturated bias is applied, the function of PG vanishes, thus the incident E_x wave is totally focused to port 2 [Fig. 4(d)]. When E_y incidents, focal spots are deflected to the right side and two spots are observed on the measured focal plane at 0 V_{rms} [Fig. 4(e)]. They combine to a single spot in the middle at 150 V_{rms} [Fig. 4(f)]. That means ports 4, 5, and 6 are consequently selected. The displacement t is measured as ±2.1 mm. Such a THz port selector can dynamically focus wave to different ports based on certain polarization and applied voltage. It may find practical applications in the future THz communications and polarization analyzers. Since the response of the LC device is proportional to the square of the LC cell gap, here the switching is limited to tens of seconds. Fortunately, the proposed THz elements still satisfy various applications where no fast switching is required. In addition, the response can be improved via optimizing the device design (e.g., stacking cells as shown in Ref. [21]) and judiciously selecting LCs.

In summary, we propose a design for active THz focusing based on an LC integrated dielectric metalens. Two specific types of metalenses are demonstrated. The first is a dual-focal metalens with bias-switched focal length. The second is a metalens with laterally shifted focal spots, and its function of a multi-port selection is verified. With above LC integrated metalenses, the three-dimensional switching of the focal spot can be realized in a non-mechanical manner. The freely programmable LC orientation enables the arbitrary geometric phase manipulation, which fully releases the freedom for dynamic THz function manipulations. This work provides a promising method for fabricating novel active THz apparatuses, which may be widely applied in THz imaging, sensing, and communication.

Funding. National Natural Science Foundation of China (61922038); Distinguished Young Scholars Fund of Jiangsu Province (BK20180004); Fundamental Research Funds for the Central Universities (14380170); Tang Scholar program.

Disclosures. The authors declare no conflicts of interest.

[†]These authors contributed equally to this work.

REFERENCES

1. H. J. Song and T. Nagatsuma, IEEE Trans. Terahertz Sci. Technol. **1**, 256 (2011).
2. S. Koenig, D. Lopez-Diaz, J. Antes, F. Boes, R. Henneberger, A. Leuther, A. Tessmann, R. Schmogrow, D. Hillerkuss, R. Palmer, T. Zwick, C. Koos, W. Freude, O. Ambacher, J. Leuthold, and I. Kallfass, Nat. Photonics **7**, 977 (2013).
3. T. Nagatsuma, G. Ducournau, and C. C. Renaud, Nat. Photonics **10**, 371 (2016).
4. F. Aieta, M. A. Kats, P. Genevet, and F. Capasso, Science **347**, 1342 (2015).
5. M. Khorasaninejad, W. T. Chen, R. C. Devlin, J. Oh, A. Y. Zhu, and F. Capasso, Science **352**, 1190 (2016).
6. M. Khorasaninejad and F. Capasso, Science **358**, eaam8100 (2017).
7. M. L. Tseng, H. H. Hsiao, C. H. Chu, M. K. Chen, G. Sun, A. Q. Liu, and D. P. Tsai, Adv. Opt. Mater. **6**, 1800554 (2018).
8. S. Wang, X. Wang, Q. Kan, J. Ye, S. Feng, W. Sun, P. Han, S. Qu, and Y. Zhang, Opt. Express **23**, 26434 (2015).
9. Z. X. Shen, S. H. Zhou, X. A. Li, S. J. Ge, P. Chen, W. Hu, and Y. Q. Lu, Adv. Photonics **2**, 036002 (2020).
10. Z. B. Fan, H. Y. Qiu, H. L. Zhang, X. N. Pang, L. D. Zhou, L. Liu, H. Ren, Q. H. Wang, and J. W. Dong, Light Sci. Appl. **8**, 1 (2019).
11. Q. Zhang, F. Dong, H. Li, Z. Wang, G. Liang, Z. Zhang, Z. Wen, Z. Shang, G. Chen, and L. Dai, Adv. Opt. Mater. **8**, 1901885 (2020).
12. S. Shrestha, A. C. Overvig, M. Lu, A. Stein, and N. F. Yu, Light Sci. Appl. **7**, 1 (2018).
13. S. Jahani and Z. Jacob, Nat. Nanotechnol. **11**, 23 (2016).
14. L. Cong, Y. K. Srivastava, H. Zhang, X. Zhang, J. Han, and R. Singh, Light Sci. Appl. **7**, 28 (2018).
15. S. H. Lee, M. Choi, T. T. Kim, S. Lee, M. Liu, X. Yin, H. K. Choi, S. S. Lee, C. G. Choi, S. Y. Choi, X. Zhang, and B. Min, Nat. Mater. **11**, 936 (2012).
16. T. Driscoll, H. T. Kim, B. G. Chae, B. J. Kim, Y. W. Lee, N. M. Jokerst, S. Palit, D. R. Smith, M. Di Ventra, and D. N. Basov, Science **325**, 1518 (2009).
17. J. Wu, B. Jin, J. Wan, L. Liang, Y. Zhang, T. Jia, C. Cao, L. Kang, W. Xu, and J. Chen, Appl. Phys. Lett. **99**, 161113 (2011).
18. X. Shen, Y. J. Wang, H. S. Chen, X. Xiao, Y. H. Lin, and B. Javidi, Opt. Lett. **40**, 538 (2015).
19. P. Chen, L. L. Ma, W. Hu, Z. X. Shen, H. K. Bisoyi, S. B. Wu, S. J. Ge, Q. Li, and Y. Q. Lu, Nat. Commun. **10**, 1 (2019).
20. Z. Zhang, Z. You, and D. Chu, Light Sci. Appl. **3**, e213 (2014).
21. L. Wang, X. W. Lin, W. Hu, G. H. Shao, P. Chen, L. J. Liang, B. B. Jin, P. H. Wu, H. Qian, Y. N. Lu, X. Liang, Z. G. Zheng, and Y. Q. Lu, Light Sci. Appl. **4**, e253 (2015).
22. S. J. Ge, P. Chen, Z. X. Shen, W. F. Sun, X. K. Wang, W. Hu, Y. Zhang, and Y. Q. Lu, Opt. Express **25**, 12349 (2017).
23. Z. X. Shen, S. H. Zhou, S. J. Ge, W. Duan, L. L. Ma, Y. Q. Lu, and W. Hu, Opt. Express **27**, 8800 (2019).
24. Z. X. Shen, S. H. Zhou, S. J. Ge, W. Duan, P. Chen, L. Wang, W. Hu, and Y. Q. Lu, Opt. Lett. **43**, 4695 (2018).
25. Z. X. Shen, S. H. Zhou, S. J. Ge, W. Hu, and Y. Q. Lu, Appl. Phys. Lett. **114**, 041106 (2019).
26. Z. X. Shen, M. J. Tang, P. Chen, S. H. Zhou, S. J. Ge, W. Duan, T. Wei, X. Liang, W. Hu, and Y. Q. Lu, Adv. Opt. Mater. **8**, 1902124 (2020).